UNIVERSITY OF AMSTERDAM

UvA-DARE (Digital Academic Repository)

Green, scalable and automated photochemistry in flow

Wen, Z.

Publication date
2022

Link to publication

Citation for published version (APA):
Wen, Z. (2022). *Green, scalable and automated photochemistry in flow*. [Thesis, fully internal, Universiteit van Amsterdam].

General rights
It is not permitted to download or to forward/distribute the text or part of it without the consent of the author(s) and/or copyright holder(s), other than for strictly personal, individual use, unless the work is under an open content license (like Creative Commons).

Disclaimer/Complaints regulations
If you believe that digital publication of certain material infringes any of your rights or (privacy) interests, please let the Library know, stating your reasons. In case of a legitimate complaint, the Library will make the material inaccessible and/or remove it from the website. Please Ask the Library: https://uba.uva.nl/en/contact, or a letter to: Library of the University of Amsterdam, Secretariat, P.O. Box 19185, 1000 GD Amsterdam, The Netherlands. You will be contacted as soon as possible.

UvA-DARE is a service provided by the library of the University of Amsterdam (https://dare.uva.nl)

Download date:14 Sept 2026

Chapter 2

A meso-scale ultrasonic milli-reactor enables gas-liquid-solid photocatalytic reactions in flow

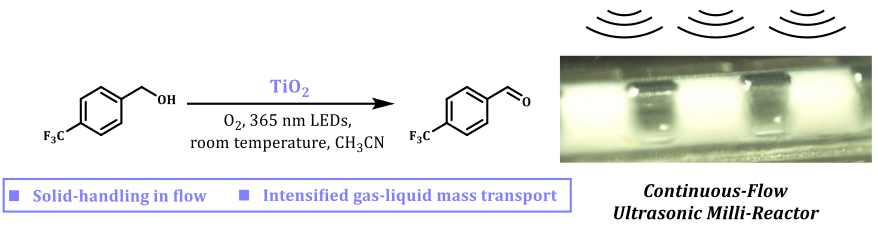

This chapter is based on:

Dong, Z.; Zondag, S. D. A.; Schmid, M.; **Wen, Z.**; Noël, T. *Chem. Eng. J.* **2022**, 428, 130968

Abstract

The handling of solid reagents, catalysts and by-products is a daunting challenge in continuous-flow micro- and milli-reactors. Suspensions tend to settle over time leading to irrevocable clogging of the reaction channels. Herein, we describe our efforts to develop an ultrasonic milli-reactor which can handle such challenging solid-containing transformations. The reactor consists of a Langevin-type transducer, a sonotrode and an irradiating cylinder, on which a coiled glass capillary (12.88 mL) was attached. The ultrasonic milli-reactor was combined with an LED illuminating box and its efficacy was showcased in the photocatalytic aerobic oxidation of benzyl alcohol enabled by TiO_2 particles exposed to UV-A irradiation. Ultrasound irradiation generates cavitation bubbles and causes a vigorous oscillation of both the cavitation and the Taylor bubbles. This improves the liquid mixing, the gas-liquid mass transfer and ensures resuspension of the settled particles. Moreover, these effects enhance the photon absorption by the semiconductor catalyst, which has an overall positive effect on the photocatalytic transformation.

2.1 Introduction

In the field of continuous flow chemistry, micro- and milli-reactors display major advantages over conventional reactors[1]. These advantages include well-controlled flow patterns and increased surface-to-volume ratios, as well as small penetration depths for photochemical applications. The resulting intensified heat and mass transfer rates, coupled with the small penetration depth, enable excellent reproducibility of the reaction conditions, and provide homogeneous irradiation of the reaction mixture, minimizing unwanted by-product formation and over-irradiation[2]. These benefits, also including enhanced safety and scalability, make this type of reactors an attractive possibility for continuous manufacturing in the chemical and pharmaceutical industry[3]. However, this reactor type lacks widespread application in industry due to the encountered weak convective mixing and commonly found problems with solid handling in flow[4].

An effective way to avoid issues with weak convective mixing (encountered mainly due to low Reynolds numbers at the small reactor dimensions) is introducing passive mixing structures (e.g., sharp bends and baffles)[5]. These microstructures, however, increase the pressure drop over the reactor and make them more susceptible to clogging. Another approach to improve the convective mixing is to utilize the internal recirculation vortices of the gas-liquid or liquid-liquid segmented flow. It has been reported that these secondary vortices could keep particles in motion and transport them in a stable three-phase flow[6]. However, as the drag force of the recirculation vortices on the particle is sometimes not strong enough to withstand the gravity force, especially when the overall flow rate is not high enough, particle sedimentation would lead to non-uniform distribution of solids and sometimes even blocking of the channel[7]. Compared to these passive methods, applying

ultrasound, as an active external force, has proven to be a more effective method to tackle those clogging and weak convective mixing issues[8]. Ultrasound irradiation generates cavitation bubbles which dance, oscillate and implode violently, giving rise to intense acoustic streaming, vortices and liquid jets[9]. These strong physical effects recirculate the solid particles and break up agglomerates, preventing solid sedimentation and bridges which ultimately cause clogging[4c,4d]. The solid handling ability of ultrasound in channels has been demonstrated for a variety of material synthetic processes and reactions which generate solid (by-)products[10]. In addition, the mixing and mass transfer enhancement of ultrasonic waves has enabled intensification of various liquid-liquid and gas-liquid processes [8,11].

Various ultrasonic micro- and milli-reactors have been reported to date. They are typically constructed by connecting the microreactor with an ultrasound transducer, which is often a Langevin-type piezoelectric element. Based on the connection method between the transducer and microreactor, two categories can be defined, i.e., directly-coupled and indirectly-coupled systems. The former directly connects the micro- or milli-reactor to the transducer surface[12], while the indirectly-coupled system utilizes a transmission medium (usually liquid) to transport ultrasound from the transducer to the reactor[13]. The easiest and often-used strategy to construct an indirectly coupled reactor is by immersing a microreactor in a commercial ultrasound cleaning bath, under which several Langevin transducers are positioned[14]. The drawback of such a setup is that the water in the bath dissipates most of the input ultrasound energy[15] and thus only a small portion is actually used to avoid clogging or to intensify mixing effects. To overcome this issue, Hübner, Jähnish et al. positioned the microreactor above the transducer in a vessel filled with pressurized water at ~4.5 bar[13a]. This suppresses the cavitation in the coupling medium and improves the ultrasound transfer efficiency.

Recently, Kuhn et al. developed a meso-scale ultrasound reactor by putting a PFA capillary in a box to which six Langevin transducers are attached[16]. The box is filled with water to transmit the ultrasound and provide temperature control. The PFA capillary has an inner diameter of 2 mm and a length of 3.81 m (internal volume 12.88 mL). These indirect coupling methods have the advantage of good temperature control and easy scale-up. However, low energy transmission efficiency, due to the attenuation in the transmission medium and reflection at the two liquid/solid interfaces, remains an issue.

In contrast, a direct coupling between transducer and reactor is a more efficient way to transport ultrasound energy. Merten et al. directly bonded a microreactor plate to the front face of a Langevin transducer with epoxy glue[12a]. A strong acoustic field was transferred into the microchannel. Following this idea, Chen et al. matched the structure of a Langevin transducer and a microreactor plate to form a half wavelength resonator in the longitudinal direction, where the antinode plane with highest sound intensity is located at the microreactor plate[17]. This novel design not only generates a uniform and strong acoustic field in the microreactor, but also maximizes the energy efficiency and lifespan of the transducer. Despite these advantages, direct coupling between transducer and reactor introduces difficulties regarding temperature control and scale-up. The ultrasound transducer will generate heat during operation, which will be guided to the microreactor directly. Moreover, as most ultrasound transducers have a limited amount of irradiated surface area, the size of the microreactor attached to it should be in the same size range. If not, non-uniform ultrasound irradiation profiles in the microreactor will be observed. For example, the transducers widely used in the ultrasonic bath utilize a cone-shaped horn to enlarge their radiating surface [9a,17]. This horn has a maximum diameter of 66 mm. When a microreactor with overall size smaller than this

diameter is attached to it, a uniform ultrasound radiation field will be formed inside the microreactor. However, if the surface area is larger, the part of microreactor not directly exposed to the ultrasound transducer will have a significantly lower ultrasound intensity. It is easy to understand that this reduces its performance and even diminishes the stability and lifespan of the reactor (due to the induction of local stress). Due to these limitations, so far, no direct-coupled ultrasound microreactors have been reported in the literature with a reactor volume larger than 2 mL.

This manuscript aims to investigate the strategies and design principle to address these scaling issues. A novel meso-scale ultrasonic milli-reactor with an irradiation surface area of 290×55 mm^2 and a reactor volume of 12.88 mL was developed. The reactor consists of a normal Langevin type transducer, a sonotrode and an irradiating cylinder, on which a coiled glass capillary was attached. Standing waves were formed in both the longitudinal direction of the sonotrode and radial direction of the cylinder. Thus, ultrasound energy is efficiently transported to the glass capillary. The temperature in the reactor can be easily controlled by two air cooling boxes wrapped around the transducer and irradiating cylinder respectively.

To validate the mixing behavior, mass transfer and solid handling performance, the reactor was applied to a three-phase photochemical reaction using solid semiconductor photocatalysts. In recent years, microflow photochemistry, and its successive scale-up, has received ample attention as it allows a homogeneous irradiation of the entire reaction medium[18]. This is challenging in conventional large-sized reactors as the light irradiance decreases exponentially with the path length (as dictated by Lambert-Beer law)[19]. As a result, photochemical transformations carried out in microreactors usually display higher

reaction selectivity and shorter reaction times. However, weak convective mixing and microchannel clogging remain important issues. Fast mixing is also important to reduce concentration gradients caused by light attenuation, which are more pronounced in larger-diameter channels (e.g., > 1 mm). In addition, many photocatalytic reactions have solid components in the reaction mixture, either as a photocatalyst (e.g., semiconductor photocatalysts)[20], as a reagent (solid bases)[21] or as a (by-) product[22]. Several solutions have been devised to handle such solid-laden flows for photochemistry, including the use of Taylor recirculation patterns[23] and oscillatory flow reactors[24] to keep the solid photocatalysts in suspension. Herein, we describe an alternative approach using a continuous-flow ultrasonic milli-reactor which can enable the UV-induced aerobic oxidation of benzyl alcohol using TiO_2 photocatalysis. Furthermore, the effects of ultrasound on the suspension behavior of the TiO_2 particles, on the hydrodynamics of the gas-liquid-solid three-phase flow and on the reaction course were investigated in detail.

2.2 Materials and methods

2.2.1 Reactor Design

Our aim was to increase the ultrasound irradiating area of a conventional sandwiched Langevin transducer and thus enable the use of larger reactor volumes. Our inspiration came from ultrasound welding tools, consisting of a normal Langevin transducer, a sonotrode and a welding head. In such tools, a standing wave is formed in the longitudinal direction, where the sonotrode transports the ultrasound energy from the transducer to the welding head. The shape of the welding head is designed to focus a large amount of energy to a specific welding point. Taking advantage of this concept, our idea was to change the welding head to a large irradiating cylinder, which is designed to resonate in the

radial direction. This would ensure that a large irradiating surface is created on the side of this cylinder, as shown in Figures 2.1(a) and (b). Following this idea, the reactor was designed as follows: First, the transducer is fixed to a standard Langevin transducer (diameter = 50 mm and total length = 120 mm) with an ultrasound frequency of 20 kHz. This frequency corresponds to a longer wavelength (240 mm) compared to other higher frequencies (such as the commonly used 28 kHz, 40 kHz and 80 kHz), allowing to irradiate a larger cylinder and thus larger ultrasound irradiating surface. The transducer consists of a back block, a front block and four piezoelectric plates which are stacked together, with a total length equaling to half a wavelength. Second, a sonotrode widely used in ultrasound welding is chosen for our design. This sonotrode has two sections, where the length of each piece equals to a quarter wavelength (60 mm). Third, the length of the irradiating cylinder was also fixed to a quarter wavelength, while the diameter is designed to match the half wavelength resonance in the radial direction.

The transducer structure was subsequently modeled using a COMSOL simulation. It was found that the resonance diameter of the irradiating cylinder is around 144 mm. As shown in the total displacement distribution in Figure 2.1(c), a standing wave is formed along the longitudinal direction of the sonotrode. The first node (from top to bottom) is positioned near the piezo stacks and the second near the center of the sonotrode. An antinode is formed at the end of the sonotrode, which could maximize the vibration excitation of the irradiating cylinder. Along the radial direction of the cylinder, minimal displacement is observed in the center while maximum at the outer surface, indicating a half-wavelength standing wave distribution. The displacement field in Figure 2.1(d) further confirms that the longitudinal vibration in the transducer and sonotrode is converted to the radial vibration in the cylinder. If a capillary tube is wrapped around the

cylinder, such a high amplitude radial vibration at the outer surface will generate a very strong ultrasound field in the tube. Therefore, this design not only enlarges the irradiation surface area by a factor 5.6 (from 28 cm^2 of the front surface area of the transducer, to 160 cm^2 at the side surface of the irradiating cylinder) but also maximizes the ultrasound energy transported to the capillary micro- or milli-reactor.

Based on this design, the reactor without capillary (the transducer, the sonotrode and the irradiating cylinder) was custom-made by Dowell Ultrasonic Tech Co. Ltd (Hangzhou, China), as shown in Figure 2.1(b). An air-cooling box was fabricated around the transducer to dissipate the heat during operation. To facilitate fixation of the reactor, an aluminum flange was connected at the center of the sonotrode where the node with minimum vibration is located. A borosilicate glass capillary with inner diameter of 2.2 mm, outer diameter of 3.9 mm and length of 4.1 m was wrapped around the outer surface of the irradiating cylinder. This forms a capillary tube milli-reactor with ten spiral loops around the cylinder and a total volume of 12.88 mL. Epoxy glue (PLUS ENDFEST 300, UHU) was used to fix the capillary on the cylinder surface and to improve the transport of the ultrasound waves from the cylinder to the capillary. As glass is a good ultrasound-conducting material, this design should allow energy supply to two or more layers of capillary wrapped around the cylinder, thus enabling even larger reactor volumes than reported herein.

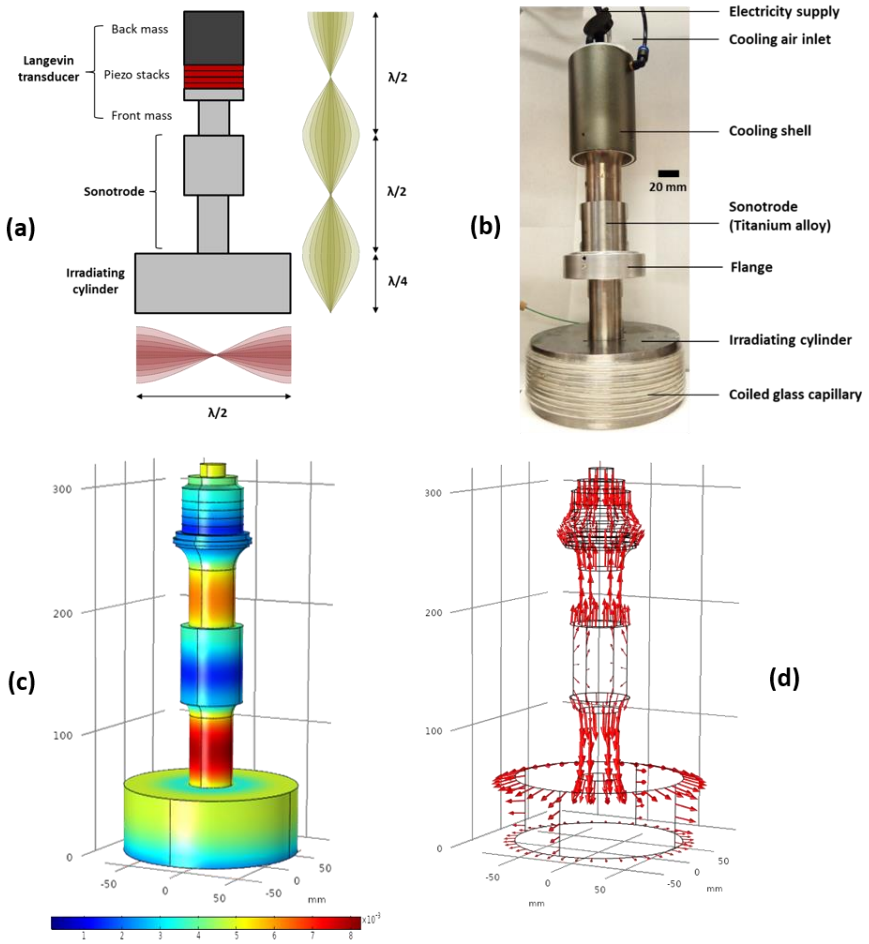

Figure 2.1 (a) Design idea of the reactor. (b) Picture of the reactor. Total displacement distribution (c) and displacement field in the reactor (d) simulated by COMSOL at resonance frequency of 20.8 kHz.

The transducer of the fabricated ultrasonic milli-reactor was actuated by an RF power amplifier (1040L, Electronics & Innovation) which is driven by a sine wave from a signal generator (DG1032Z, Rigol). An impedance transformer (JT-450, Electronics & Innovation) was connected between the power amplifier and the transducer to match the impedance difference, minimizing the reflected power from the transducer[9a]. By sweeping the driving frequency of the sine wave from the signal generator around the designed frequency (20.8 kHz), the frequency corresponding to the largest electric load power displayed on the power

amplifier was determined as the optimal working frequency of the ultrasonic milli-reactor. The optimal frequency was found to be 22.6 kHz, which is 9% higher than the designed frequency predicted by COMSOL simulation. This deviation could be caused by the small structural differences between the actual reactor and the modelled reactor. During fabrication of the reactor, there were inevitable deviations between the designed size and the actual size of each part. In addition, the COMSOL model did not account for the connecting screws, the glass capillary, the cooling shell and the flange of the actual reactor.

2.2.2 Application of the ultrasonic milli-reactor in heterogeneous photocatalysis

Next, the application potential of this transparent glass capillary milli-reactor was showcased in solid-laden photocatalytic reactions enabled by semiconductor-based photocatalysis [19b,25]. As a benchmark reaction, the photocatalytic oxidation[26] of 4-(trifluoromethyl)benzyl alcohol using TiO_2 and gaseous oxygen subjected to UV-A light (365 nm) was selected (Scheme 2.1)[27]. An LED box was constructed in which the UV-A LED strip was fixated and where the ultrasound cylinder and glass capillary can be positioned (Figure 2.2). The box was made of a stainless-steel pipe with an inner diameter of 200 mm, a wall thickness of 1.75 mm and a height of 150 mm (Figure 2.2b). A UV-A LED strip (365 nm, LS24UV240X2835PLX, LuxaLight) with a length of 3 m was attached to the inner surface of the pipe. In the cover, there are holes to allow for milli-fluidic connections and the supply of cooling air. The LED strip was powered by a DC power supply (LABPS3005D, Velleman). The applied voltage and current were 24 V and 2.7 A respectively, resulting in an electric power consumption of 64.8 W for the LED strip. The working frequency of the ultrasonic transducer was 22.6 kHz and the load power was typically around 60 W.

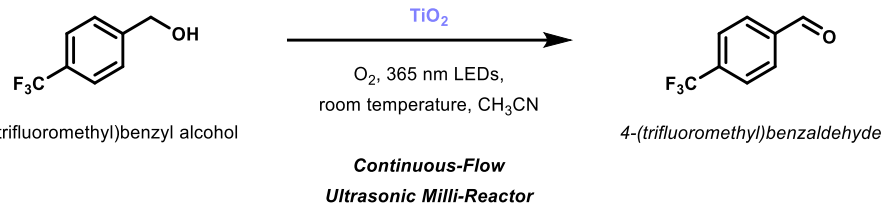

Scheme 2.1 Photocatalytic oxidation of 4-(trifluoromethyl)benzyl alcohol using TiO_2 and O_2, selected as a benchmark reaction for the evaluation of the continuous-flow ultrasonic milli-reactor.

A stock solution was prepared by suspending TiO_2 nanoparticles (Titanium oxide, anatase, <25 nm, 637253-50G, Sigma-Aldrich) in a solution of 4-(trifluoromethyl)benzyl alcohol (SC034058, Fluorochem Limited) in acetonitrile (MeCN, HPLC-R, Biosolve Chimie SARL). For the exact concentrations, we refer to the corresponding experiments (see section 2.3.2). The TiO_2 particles were smaller than 25 nm, which is, however, the initial size of these particles. The actual powder consists of aggregates and agglomerations of these primary particles. The actual particle size distribution of TiO_2 particles in the solution was measured by a laser particle sizer (Analysette 22 microtec plus, Fritsch). As shown in Figure S2.1, the measured size distribution shows a wide distribution with three agglomeration peaks, falling in the range of 0.1-1, 1-10 and 10-40 μm respectively. The average size is 3.8 μm. Next, the stock solution was taken up in a 60 mL plastic syringe, in which a magnetic stir bar was placed. The syringe was mounted on a syringe pump (Fusion 720, Chemyx Inc.). Magnetic stirring was applied by putting a compact magnetic stirrer (Topolino, IKA) beneath the front part of the syringe (as shown in Figure 2.2). In this way a uniform suspension was maintained inside the syringe and was infused into the ultrasonic milli-reactor. To prevent particles settling down at the inlet microfluidic connections, these connections were kept as short as possible (ca. 5 cm) and were placed in a downward trajectory before reaching the reactor. The gas phase was fed from an oxygen gas line and dosed into the liquid stream

using a mass flow controller (F-200CV-002-AAD-22-K, Bronkhorst Nederland BV). The gas and liquid phase were combined in a stainless-steel tee junction (VALCO) to establish a gas-liquid Taylor flow regime and were subsequently delivered to the photochemical ultrasonic milli-reactor. Therefore, a gas-liquid-solid three phases flow was formed in the milli-channel, which was exposed to the UV light. The physical properties of the three phases are listed in Table 2.1.

Table 2.1 Physical properties of the three phases (gas, liquid and solid) in the milli-reactor. The liquid phase was treated as pure acetonitrile, considering the substrate concentration is very low (1-5 mM).

Phase	Composition	Density (g/cm^3)	Viscosity (mPa·s)	Flow rate (mL/min)	Reynolds number (Re)	Capillary number (Ca) $\times 10^{-3}$	Weber number (We) $\times 10^{-3}$
Gas	O_2	0.0014	0.020	0.05-0.19	6.42-25.7		
Liquid	MeCN	0.786	0.334	0.19-0.75	0.76-3.1	0.009-0.04	0.04-0.15
Solid	TiO_2	4.23			0.009-0.036		

During the experiments, both the operation of the UV light strip and the ultrasound transducer generate heat. To cool the reactor, a stream of compressed air was introduced into the assembly. A thermocouple was inserted into the outlet of the glass capillary which allowed to measure the temperature in the reaction mixture. When the LED light was turned on, the temperature raised from room temperature (22.6 °C) up to 28.5 °C. When both the ultrasound and LED light were switched on, the temperature was further increased to 39.2 °C, equaling to a rise of 10.7 °C caused by ultrasound. Such a high temperature rise would influence the reaction rate substantially, which might interfere with the study of the physical effects of ultrasound. To prevent this, a pulsed ultrasound of ON/OFF time of 12.5/12.5 s instead of a continuous ultrasound

generation was applied. Such a pulsed ultrasound only generates half of the heat and allows for a more rigorous cooling of the entire setup. In this way, a temperature of 31.4 °C was measured, which means that the pulsed ultrasound only increases the temperature by 2.9 °C. This quite small temperature increase should allow for an excellent description of the ultrasound effects on the reaction. Moreover, to exclude the direct chemical effect of ultrasound (e.g., sonolysis) on the reaction, a control experiment was conducted when ultrasound is turned ON and light turned OFF. Also, another experiment with both ultrasound and light turned OFF was executed. No conversion was detected in either control experiments, demonstrating that this is indeed a photocatalytic transformation.

Samples of the reaction were collected at the reactor outlet after the reactor was in continuous operation for at least 2 residence times to ensure steady-state data collection. ^{19}F-NMR was used to analyze the ratio of the product and substrate in the samples, based on which the conversion and selectivity were calculated. The TiO_2 particles were first removed by filtering the sample with a 0.22 μm syringe filter. The sample was diluted with deuterated chloroform ($CDCl_3$, SC040234, Deutero GmbH) in a ratio of 1:1 and measured on a Bruker 400 MHz NMR spectrometer. Three samples were collected and measured separately for each experimental condition. The deviation of conversion and selectivity in all the repeated experiments was less than 2%.

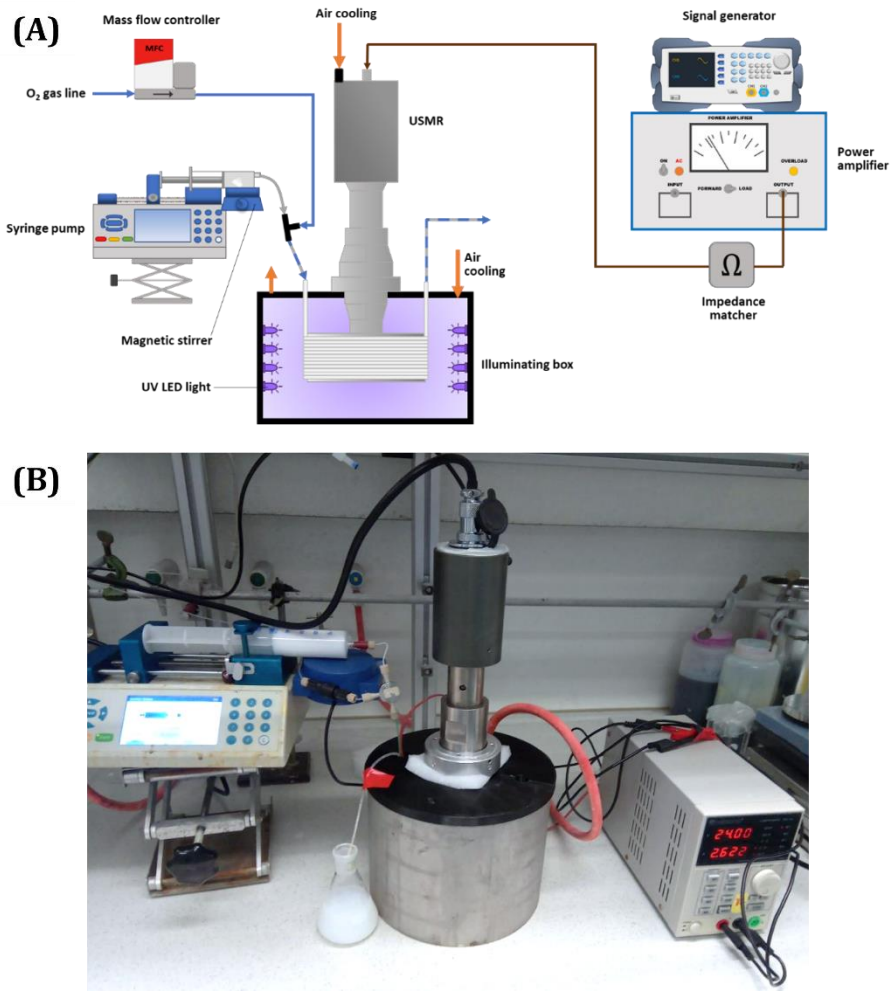

Figure 2.2 (A) Schematic representation of the experimental setup. (B) Picture of the setup, which shows the ultrasonic reactor with illuminating box in the middle and syringe pump on the left.

2.3. Results and discussions

2.3.1 Ultrasound effects on the gas-liquid-solid three-phase flow

To study the effect of ultrasound on the hydrodynamics of the three-phase flow, the ultrasonic reactor was first run without exposing it to UV light. A liquid solution containing 10 mg/mL TiO_2 in acetonitrile was merged with pure oxygen and the combined three-phase flow was

introduced in the reactor. Images of the three-phase flow in the glass capillary were taken by a high-speed camera (AOS L-PRI 1000) with a macro lens (Canon EFS 60 mm). The camera was faced to the capillary reactor from the side, while a high intensity LED-based light source (Veritas Constellation 120E15) was illuminating from the top of the reactor. As shown in Figures 2.3 (a) and (c), the TiO_2 particles rapidly settled down in the reactor when no ultrasound was applied (at a total gas-liquid flow rate of 2 mL/min). Remarkably, most particles were already sedimented at the first and second spiral loop. The number of suspended particles reduces with increasing reactor length, with almost no particles visible in the capillary from the third winding onwards. The same observation holds for the solution sample collected at the outlet (Figure 2.5). This implies that the particles completely settle after about 92 cm (two spiral loops); from this observation, a sedimentation time of 105 s can be estimated. This roughly estimated value is in the same order of magnitude with the theoretical time (27 s) calculated from the Stokes' sedimentation equation, for which the average particle size of 3.8 μm was used (See experimental section). It should be noted that a gradual decline of the amount of TiO_2 over the reactor length will lead to a sub-optimal photocatalytic process (see section 2.3.2) and should eventually lead to reactor clogging in those first two reactor loops.

When ultrasound was applied, the particles were re-suspended within a few seconds, showing that the sedimentation process is reversible and that reactor clogging can be prevented. A uniform and milky liquid phase was observed in both the capillary (Figures 2.3(b) and (d)) and in the outlet sample (Figure 2.5). The re-suspending of the TiO_2 particles was caused by the cavitation bubbles and the surface wave oscillation of the Taylor bubbles induced by the ultrasound irradiation, as shown in Figure 2.3(f). The cavitation bubbles moved randomly and oscillate vigorously in the liquid slug, acting as micro-stirrers to mix the liquid and solids. This

mixing effect of cavitation bubbles in the reactor has been systematically investigated in previous work[9a]. At the same time, surface wave oscillations of the oxygen Taylor bubble were also induced, resulting in a crinkly bubble surface (Figure 2.3(f)) compared to the original smooth surface (Figure 2.3(e)) when ultrasound is not applied. Such a surface wave oscillation produces cavitation microstreaming around the bubble, improving the liquid mixing and gas-liquid mass transfer[28]. Further analysis of the high-speed video shows that it only takes 2 s for the ultrasound effects to re-suspend the particles. As shown in Figure 2.4, at the moment prior to ultrasound application (i.e., 0.0 s), TiO_2 particles were settled at the bottom of the glass capillary. 0.2 s after ultrasound actuation was switched on, cavitation microstreaming started to mix the particles and recirculate them in the liquid slug. With the increase of the ultrasound irradiation time, gradually more particles were re-suspended. After about 2 s, a uniform liquid suspension was observed in all the liquid slugs.

All the experiments in Figures 2.3 and 2.4 applied a continuous ultrasound wave with an electronic power of 60 W. Such a continuous application of ultrasound resulted in a temperature rise of 10.7 °C, which would influence the reaction rate significantly. To avoid this problem, pulsed ultrasonication was applied. Previous work on $CaCO_3$ particle synthesis showed that pulsed ultrasonication with an ON/OFF time of 7.5/12.5 s was able to generate similar effects on mixing and agglomeration breakup compared to continuous ultrasonication[10d].

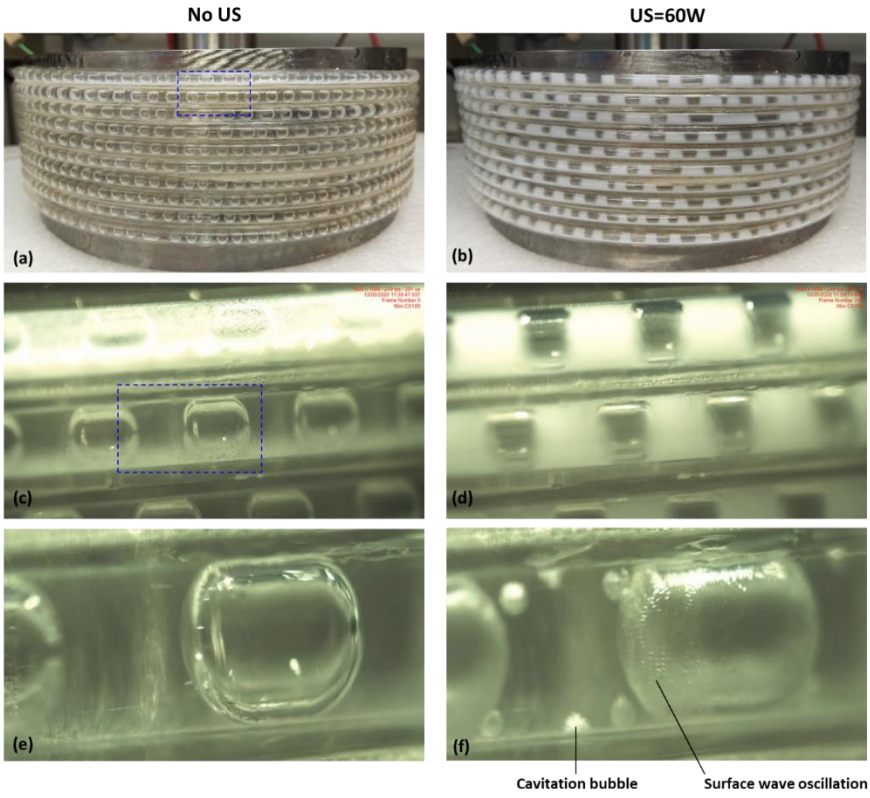

Figure 2.3 Effect of ultrasound on the three-phase flow in the glass capillary reactor. Images on the left (a, c, e) were taken without ultrasound actuation, while the right ones (b, d, f) were under continuous ultrasound irradiation at a power of 60 W. In all images the gas phase is oxygen and the liquid phase is acetonitrile, with or without suspended TiO_2. Both (a) and (b) are the full view of the reactor, where (c) and (d) are the zoomed view of a section of the first three spirals as indicated by the blue dashed rectangle in (a). The acetonitrile in (a, b, c, d) contains 10 mg/mL TiO_2. Both (e) and (f) used pure acetonitrile and are shown using the zoomed view of a section of the second spiral, as indicated by the blue dashed rectangle in (c). The flow rate of the gas and liquid/suspension phase were both 1 mL/min in image (a) and (b). While from images (c) to (f), the flow rate was respectively 0.8 and 0.6 mL/min for the gas and liquid/suspension phase.

Herein, to ensure similar particle re-suspension performance compared to continuous ultrasound, the ON period of the pulsed ultrasonication has to be longer than the ultrasound-induced resuspension time (2 s), while the OFF period should be shorter than the experimental and theoretical sedimentation time of the TiO_2 particles (88 s and 27 s, respectively). Considering all these effects, an ON/OFF time of 12.5/12.5 s was selected in the following reaction experiments. The power applied in the ON

period is 60 W, resulting in an effective power applied of 30 W. Such a pulsed ultrasonication results in a much lower temperature rise (i.e., 2.9 °C) compared to continuous ultrasound application. Importantly, this pulsed ultrasonication was able to re-suspend the TiO_2 particles equally well as the continuous application of ultrasound. This is further confirmed by the pictures of the samples collected at the reactor outlet as shown in Figure 2.5. Both samples, collected under pulsed and continuous ultrasound, are uniformly milky with no visible differences.

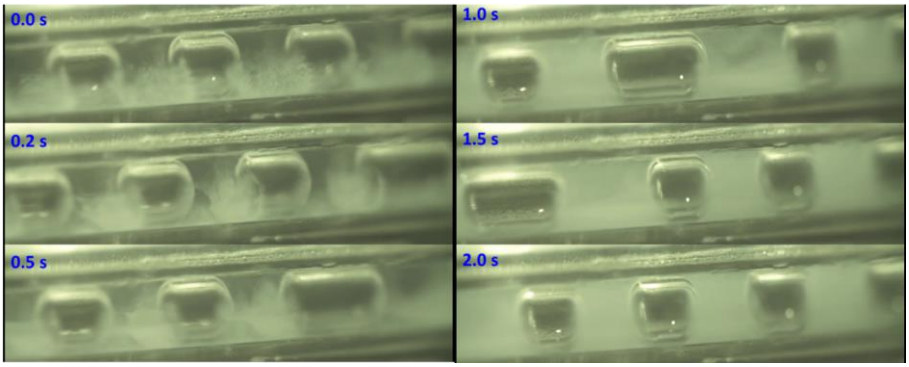

Figure 2.4 Single frames of a video showing that ultrasound allows to re-suspend the sedimented TiO_2 particles to a visibly homogeneous suspension within a period of 2.0 seconds after switching on the ultrasound. Experimental conditions are equal to those in Figure 2.3(c).

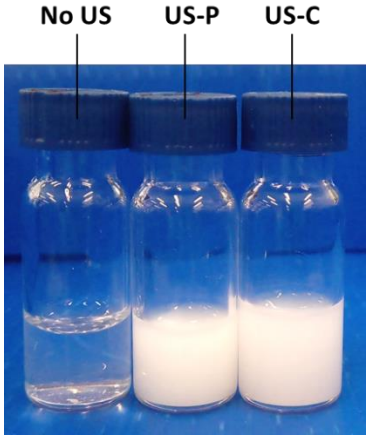

Figure 2.5 Images of the reaction samples collected at the reactor outlet under the condition of no ultrasound, pulsed ultrasound (US-P) and continuous ultrasound (US-C).

2.3.2 Ultrasound effects on the reaction conversion

In the previous section, our results demonstrated that ultrasound irradiation generates cavitation bubbles and activates the surface wave oscillations of the Taylor bubbles, which improves the mixing in the liquid slug and re-suspends the TiO_2 particles. These effects are expected to improve the reaction rate of the photocatalytic oxidation of 4-(trifluoromethyl)benzyl alcohol using TiO_2 and O_2 to the corresponding benzaldehyde (Scheme 2.1).

Indeed, the conversions obtained under ultrasound irradiation were always higher than those without (Figure 2.6). The highest conversion improvement, i.e., 3.6 times, was observed at substrate concentrations of 1 mM and a TiO_2 concentration of 5 mg/mL. The influence of ultrasound on the selectivity is not significant and is mainly dependent on the conversion. The selectivity is higher than 95% when the conversion is lower than 40% and reduces to around 85% when the conversion exceeds 60%. The main byproduct is the corresponding benzoic acid, derived from over-oxidation[26b,29]. The effect of ultrasound on the conversion at different residence times and TiO_2 concentrations was investigated as well, as shown in Figure 2.7. When the ultrasound is switched off, the conversion reduces from 57% to 24% when the residence time was increased from 14 to 55 min. Such a reduction of conversion with residence time can be attributed to the sedimentation of TiO_2 particles in the reactor. Longer residence times correspond to lower flow rates, resulting in a shorter reactor length over which the particles settle. This gives a lower effective reactor volume where the TiO_2 particles are well suspended and thus where TiO_2-mediated photocatalysis occurs, resulting in lower conversion. In contrast, when ultrasound is applied, the conversion increases from 71% to 86% when the residence time is increased from 14 min to 28 min. A further increase of the residence time to 55 min does not improve the conversion further. This indicates that light absorption is not limited anymore from 28 min

onwards. Finally, the conversion under no ultrasound increased slightly (7%) when the TiO_2 concentration was increased from 1 to 5 mg/mL. When ultrasound was applied, the conversions were 3.0-3.6 times higher compared to the case without ultrasound. In this case, a much higher increase of conversion (37%) was observed when the TiO_2 concentration increased from 1 to 5 mg/mL.

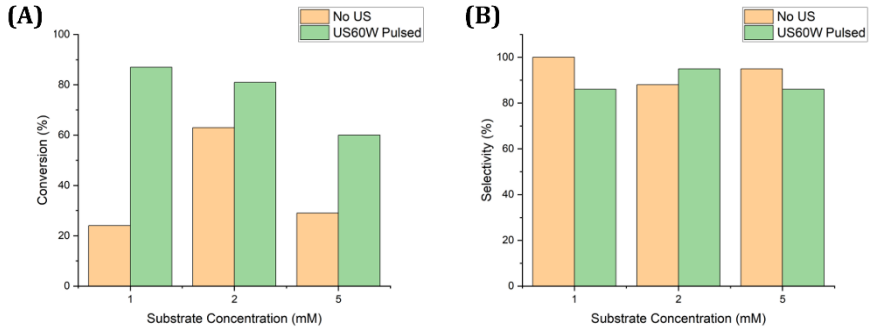

Figure 2.6 The effect of ultrasound on the conversion (A) and selectivity (B) in the 4-(trifluoromethyl)benzyl alcohol using TiO_2 and O_2 for different substrate concentrations. The concentration of TiO_2 was 5 mg/mL. Residence time was 55 min. The gas-to-liquid volumetric flow rate ratio was 0.25.

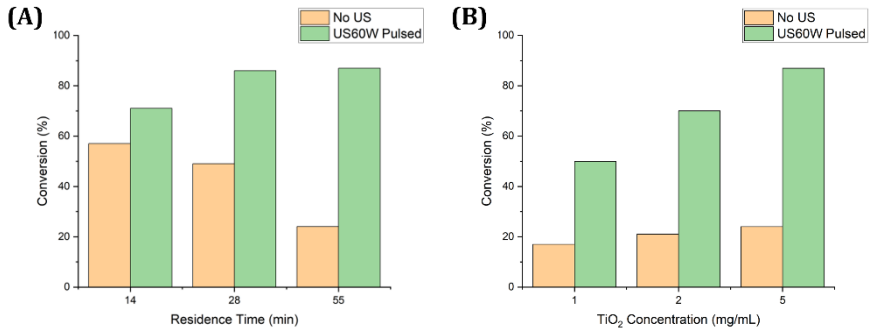

Figure 2.7 The effect of ultrasound on the conversion at different residence times (A) and TiO_2 concentrations (B). The concentration of TiO_2 and substrate in (A) was 5 mg/mL and 1 mM respectively. While in (B), the residence time was 55 min and the substrate concentration was 1 mM. The gas-to-liquid volumetric flow rate ratio was fixed to 0.25 in all the experiments.

Such a significant increase in conversion under ultrasound irradiation can be rationalized to the improvement of several mass-transfer-related processes. The photocatalytic aerobic oxidation reaction depends on the

supply of oxygen from the gas phase to the catalyst surface; it is known that ultrasound can increase this critical mass transfer rate at the gas-liquid interface by a factor of 3 to even 20[17,27,28a]. However, also liquid-solid mass transfer plays a critical role, as well as the exposure of the catalyst to the light. These are individual steps where the mass transfer rates can be efficiently increased by the oscillation of the cavitation bubbles and the surface wave oscillations at the O_2 gas bubbles in the Taylor flow regime. The sonication ensures maximum irradiation efficiency and provides a uniform suspension of the titanium oxide inside the liquid medium. Finally, ultrasound impedes effectively settling and agglomeration effects of the catalyst that would reduce the catalytically accessible active surface of the catalyst. Although ultrasound irradiation could improve the gas-liquid, liquid-solid mass transfer and photon absorption by the catalyst surface at the same time, the main contribution to the conversion enhancement should be attributed to the rate limiting step. Mass transfer correlations reported in literature[7c,30] were adopted to estimate the mass transfer rate in our experiment (See Supporting Information). The estimated gas-liquid and liquid-solid mass transfer coefficients are 0.12-0.62 and 4017-4211 s^{-1} respectively, indicating that the mass transfer processes are in the time scale of 1-10 s and 0.1-1 ms respectively. Both are much faster than the time scale of the reaction (14-55 min). Therefore, compared to the mass transfer processes, photon absorption by the catalyst is more likely to be the rate-limiting step. The conversion enhancement by ultrasound irradiation should be mainly attributed to the improvement of catalyst surface's exposure to the light.

2.4. Conclusion

Herein, we presented the development of a robust and efficient meso-scale ultrasonic milli-reactor with a reactor volume of 12.88 mL, which can be used to carry out solid-laden photochemical transformations. The

reactor consists of a Langevin-type transducer, a sonotrode and an irradiating cylinder, on which a coiled glass capillary was attached. Standing waves were formed in both the longitudinal direction inside the sonotrode and radial direction inside the cylinder, efficiently directing the ultrasound energy to the glass capillary. The ultrasonic milli-reactor was combined with an LED illuminating box and its efficacy was showcased in the aerobic oxidation of 4-(trifluoromethyl)benzyl alcohol catalyzed by TiO_2 particles under UV light irradiation. Ultrasound irradiation generates cavitation bubbles and causes a vigorous oscillation of both cavitation bubbles and the Taylor bubbles, which improves the liquid mixing, the gas-liquid mass transfer and ensures resuspension of the settled particles in 2 s. Ultrasound enabled recirculation of the suspended TiO_2 nanoparticles and break-up of the agglomerates. These effects enhance the photon absorption by the semiconductor catalyst, improving the reaction conversion with a factor of 3.6.

We believe that the outlined scale-up strategy and design principle of the meso-scale ultrasonic milli-reactor and its successful performance for photocatalysis will spur further research into other large-scale ultrasound-enabled reactor development. Moreover, this reactor can be applied in various – not necessarily photocatalytic – multiphase reactions, especially those involving solids and with risks of clogging.

2.5 Experimental section

2.5.1. Particles size distribution of the TiO_2 power

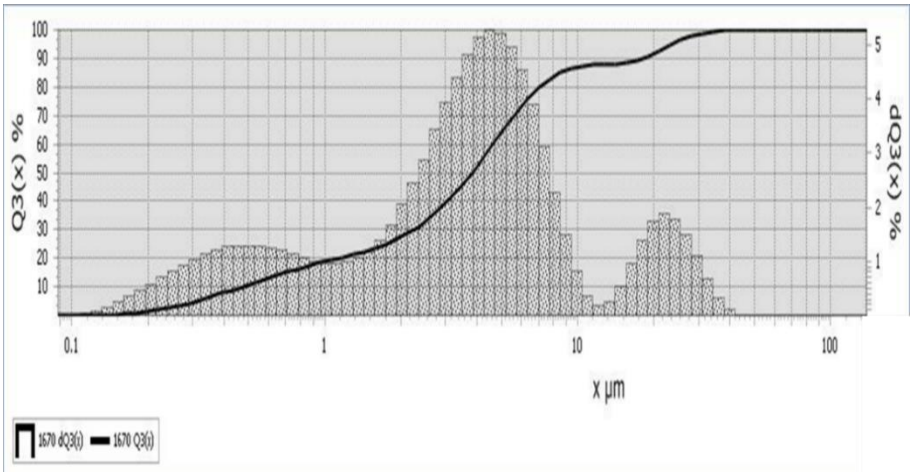

Figure S2.1 The measured particle size distribution of TiO_2 power in the solution. Columns are the density distribution and the solid curve is the cumulative distribution.

The particle size distribution of TiO_2 power in the solution was measured by a laser particle sizer (Analysette 22 microtec plus, Fritsch). A CH_3CN solution with 5 mg/ml TiO_2 power and 1 mM of substrate was used.

2.5.2. COMSOL simulation

A COMSOL Multiphysics model was created for the 3D geometrical ultrasonic tool. The materials assigned to the different parts of the geometry are as follows; Steel AISI 4340 for the back mass, Titanium beta-21S for the front mass and Lead Zirconate Titanate (PZT-4) for the ceramic piezoelectric disks. The manufactured sonotrode contains a pre-stressed steel bolt through the four ceramic disks, but in the model this bolt is not included, and the ceramic disks are assumed to be whole instead of being drilled. The applied potential to the interface of these disks is set at 10 V. Another difference between the manufactured and modelled sonotrode is the central disk (bored cylinder) which is used for the suspension of the sonotrode in the reactor casing, the flange. This

flange is screwed into the titanium cylinder of the sonotrode, but with intentionally some space left in between the surfaces, resulting in only a small interface between the two assembled parts. It is assumed that this small interface will not significantly affect the behavior of the model and is only included in the manufactured sonotrode for ease of use. Since the model does not consider the heating of the sonotrode, also the cooling shell is not included in the geometrical representation. The model was made without the addition of the coiled glass capillary on the irradiating cylinder surface, which was only attached to the sonotrode after manufacturing. Since this capillary becomes part of the solid structure, this could affect the observed resonance frequency and contribute to a deviation between the simulated and observed frequency.

Solving the set of equations for the included Electrostatics and Solid Mechanics of the considered Physics subparts was done by means of the built-in Finite Element Method, where the fine mesh was generated by the software. The resonance frequency that was found by the execution of this model, using an eigenfrequency Study, was 20.8 kHz.

2.5.3 Estimation of the gas-liquid and liquid-solid mass transfer rate

The gas-liquid mass transfer rate was estimated from the correlation reported by Yue et al[30], which is a classic paper on gas-liquid mass transfer in microchannel. They proposed the following correlation to predict gas-liquid mass transfer coefficient of segmented flow:

$$k_{\mathrm{L}}a = 0.084 Re_{\mathrm{G}}^{0.213} Re_{\mathrm{L}}^{0.937} Sc_{\mathrm{L}}^{0.5} \frac{D_{\mathrm{m}}}{D^2} \qquad \textbf{Eq}.\ 2.1$$

Inserting the physical properties and Reynolds numbers shown in table 1, a $k_{\mathrm{L}}a$ in the range of 0.12-0.62 s^{-1} was obtained, which is close to the experimental measurement results (0.1-0.4 s^{-1}) in a similar gas-liquid two-phase flow in our previous research[28a].

The liquid-solid mass transfer of particles suspended in gas-liquid segmented flow was rarely reported in literature. Fortunately, A.K. Liedtke et al. have done systematical research on it[31]. The following correlation was proposed to predict the external liquid-solid mass transfer coefficient (k_S):

$$Sh = \frac{k_S d_p}{D_{m,L}} = 2 + 0.30 Re_p^{0.5} Sc_L^{1/3} \quad \textbf{Eq. 2.2}$$

In which Sh is the Sherwood number, $Re_p = \rho_L U_{TP} d_p / \mu_L$ is the Reynolds number for the particle. Assuming a TiO_2 particle is a perfect sphere and its specific surface area is equal to $3/d_p$, combing with the above equation gives the following correlation to predict the overall liquid-solid mass transfer coefficient:

$$k_S a = \frac{3 D_{m,L}}{d_p^2} \left(2 + 0.30 Re_p^{0.5} Sc_L^{1/3}\right) \quad \textbf{Eq. 2.3}$$

Inserting the values shown in Table 1, an overall mass transfer coefficient in the range of 4017-4211 s^{-1} was obtained.

2.6 Associated content

Further experimental details are available as Supporting Information published on the Chemical Engineering Journal website with DOI: 10.1016/j.cej.2021.130968.

2.7 Reference

1. (a) K.F. Jensen, AIChE J. **2017**, *63,* 858-869. (b) K. Jahnisch, V. Hessel, H. Löwe, M. Baerns, *Angew. Chem. Int. Ed.* **2004**, *43,* 406-446. (c) P. Plouffe, A. Macchi, D.M. Roberge, *Org. Process Res. Dev.* **2014**, *18* 1286–1294.
2. (a) B. Gutmann, D. Cantillo, C.O. Kappe, *Angew. Chem. Int. Ed.* **2015**, *54,* 6688–6728. (b) L. Rogers, K.F. Jensen, *Green Chem*. **2019**, *21*, 3481–3498. (c) J. Yoshida, H. Kim, A. Nagaki, *ChemSusChem.* **2011**, *4,* 331-340. (d) C. Sambiagio, T. Noël, *Trends Chem*. **2020**, *2*, 92-106.
3. (a) M. Berton, J.M. de Souza, I. Abdiaj, D.T. McQuade, D.R. Snead, *J. Flow Chem.* **2020**, *10*, 73–92. (b) R. Moylan, S. Bourke, K. Cole, S. May, **2020**, RSC publishing. (c) V. Hessel, D. Kralisch, N. Kockmann, T. Noel, Q. Wang, *ChemSusChem,* **2013**, *6* 746-789. (d) K.P. Cole, J.M. Groh, M.D. Johnson, C.L. Burcham, B.M. Campbell, W.D. Diseroad, et al., *Science* **2017**, *356,* 1144-1150. (e) N. Kockmann, *ChemBioEng Rev* **2016**, *3*, 1-12. (f) S. Govaerts, A. Nyuchev, and T. Noël, *J. Flow Chem*. **2020**, *10*, 13-71.
4. (a) K. Wu, S. Kuhn, *Chim. Oggi Chemistry Today,* **2014**, *32*, 62–67. (b) M. Schoenitz, L. Grundemann, W. Augustin, S. Scholl, *Chem. Commun*. **2015**, *51*, 8213-8228. (c) R. L. Hartman, J.R. Naber, N. Zaborenko, S.L. Buchwald, K.F. Jensen, *Org. Process Res. Dev.* **2010**, *14*, 1347-1357. (d) R. L. Hartman, *Org. Process Res. Dev.* **2012**, *16*, 870-887.
5. (a) V. Hessel, H. Löwe, F. Schönfeld, *Chem. Eng. Sci*. **2005**, *60*, 2479-2501. (b) M.N. Kashid, A. Renken, L. Kiwi-Minsker, Wiley-VCH Verlag GmbH & Co. KGaA: Weinheim, Germany, **2014**.
6. (a) D.I. Enache, G.J. Hutchings, S.H. Taylor, R. Natividad, S. Raymahasay, J.M. Winterbottom, E.H. Stitt, *Ind. Eng. Chem. Res*. **2005**, *44*, 6295–6303. (b) D.I. Enache, G.J. Hutchings, S.H. Taylor, E.H. Stitt, *Catalysis Today* **2005**, *105*, 569-573. (c) A. Ufer, D. Sudhoff, A. Mescher, D.W. Agar, *Chem. Eng. J.* **2011**, *167*, 468-474. (d) A.K. Liedtke, F. Bornette, R. Philippe, C. de Bellefon, *Chem. Eng. J.* **2013**, *227* 174-181. (e) K. Olivon, F. Sarrazin, *Chem. Eng. J.* **2013**, *227*, 97-102.
7. (a) D.I. Enache, G.J. Hutchings, S.H. Taylor, S. Raymahasay, J.M. Winterbottom, M.D. Mantle, A.J. Sederman, L.F. Gladden, C. Chatwin, K.T. Symonds, E.H. Stitt, *Catal. Today,* **2007**, *128*, 26-35. (b) A.K. Liedtke, F. Scheiff, F. Bornette, R. Philippe, D.W. Agar, C. de Bellefon, *Ind. Eng. Chem. Res.* **2015**, *54*, 4699-4708. (c) A.K. Liedtke, F. Bornette, R. Philippe, C. de Bellefon, *Chem. Eng. J.* **2016**, *287*, 92-102.
8. (a) R.D. Fernandez, S. Kuhn, *Top. Curr. Chem*. **2016**, *70*, 374. (b) Z. Dong, C. Delacour, K.M. Carogher, A. Udepurkar, S. Kuhn, *Materials* **2020**, *13*, 344.
9. (a) Z. Dong, S. Zhao, Y. Zhang, C. Yao, Q. Yuan, G. Chen, *AIChE J*. **2016**, *63*, 1404-1418. (b) R.D. Fernandez, P. Cintas, H.J.G.E. Gardeniers, *Chem.*

Commun. **2012**, *48*, 10935-10947. (c) A. Ozcelik, D. Ahmed, Y. Xie, N. Nama, Z. Qu, A.A. Nawaz, T.J. Huang, *Anal. Chem*. **2014,** *86*, 5083-5088.

10. (a) C. Delacour, C. Lutz, S. Kuhn, *Ultrason. Sonochem.* **2019**, *55*, 67-74. (b) T. Noël, J.R. Naber, R.L. Hartman, J.P. Mcmullen, K.F. Jensen, S.L. Buchwald, *Chem. Sci.* **2011**, *2*, 287-290. (c) Z. Dong, R.D. Fernandez, S. Kuhn, *Lab Chip* **2019**, *19*, 316-327. (d) Z. Dong, A. Udepurkar, S. Kuhn, *Ultrason. Sonochem.* **2020**, *60*, 104800. (e) G. Laudadio, H.P. L. Gemoets, V. Hessel, T. Noel, *J. Org. Chem.* **2017**, *82*, 11735-11741.
11. S. Zhao, C. Yao, Z. Dong, G. Chen, Q. Yuan, *Particuology* **2020**, *48*, 88-99.
12. (a) Q. Tseng, A. M. Lomonosov, E. E. M. Furlong, C. A. Merten. *Lab Chip* **2012**, *12*, 4677-4682. (b) J.J. John, S. Kuhn, L. Braeken, T.V. Gerven. *Chem. Eng. Process* **2016**, *102*, 37–46. (c) S. Kuhn, T. Noël, L. Gu, P.L. Heider, K.F. Jensen, *Lab Chip* **2011**, *11*, 2488-2492.
13. (a) S. Hübner, S. Kressirer, D. Kralisch, C. Bludszuweit-Philipp, K. Lukow, I. Jänich, A. Schilling, H. Hieronymus, C. Liebner, K. Jähnisch, *ChemSusChem* **2012**, *5*, 279-288. (b) I. Iranmanesh, M. Ohlin, H. Ramachandraiah, S. Ye, A. Russom, M. Wiklund, *Biomed. Microdevices* **2016**, *18*, 1-7. (c) D. Roberge, F. Raimone, W. Quittmann, M. Gottsponer, M. Eyholzer, *US20150158007A1*, 11 June **2015**.
14. (a) T. Horie, M. Sumino, T. Tanaka, Y. Matsushita, T. Ichimura, J.-I. Yoshida, *Org. Process Res. Dev.* **2010**, *14*, 405-410. (b) S. Aljbour, T. Tagawa, H. Yamada, *J. Ind. Eng. Chem.* **2009**, *15*, 829-834.
15. R. Van Zwieten, B. Verhaagen, K. Schroën, D. Fernández Rivas, *Ultrason. Sonochem*. **2017**, *36*, 446-453.
16. C. Delacour, D. Stephens, C. Lutz, R. Mettin, S. Kuhn, *Org. Process Res. Dev.* 2020, 24, 2085-2093.
17. Z. Dong, C. Yao, X. Zhang, J. Xu, G. Chen, Y. Zhao, Q. Yuan, *Lab Chip*, **2015**, *15*, 1145-1152.
18. (a) D. Cambié, C. Bottecchia, N.J.W. Straathof, V. Hessel, T. Noël, *Chem. Rev.* **2016**, *116*, 10276-10341. (b) B. Wriedt, D. Ziegenbalg, *J. Flow Chem*. **2020**, *10*, 295-306. (c) Donnelly, K., Baumann, M. *J Flow Chem* **2021**, *11*, 223-241.
19. (a) Y. Su, N.J.W. Straathof, V. Hessel, T. Noel, *Chem. Eur. J.* **2014**, *20*, 10562-10589. (b) K. Loubière, M. Oelgemöller, T. Aillet, O. Dechy-Cabaret, L. Prat, *Chem. Eng. Process* **2016**, *104*, 120-132.
20. P.R. Paiva, T. Noel, *Catal. Sci. Technol*. **2019**, *9*, 5186-5232.
21. A.V. Nyuchev, T. Wan, B. Cendón, C. Sambiagio, J.J.C. Struijs, M. Ho, M. Gulías, Y. Wang, T. Noël, *Beilstein J. Org. Chem.* **2020**, *16*, 1305-1312.
22. R.T. Smith, X. Zhang, J.A. Rincón, J. Agejas, C. Mateos, M. Barberis, S. García-Cerrada, O. Frutos, D.W.C. MacMillan, *J. Am. Chem. Soc.* **2018**, *140*, 17433-17438.

23. B. Pieber, M. Shalom, M. Antonietti, P.H. Seeberger, K. Gilmore, *Angew. Chem. Int. Ed.* **2018**, *57*, 9976.
24. P. Bianchi, J. Williams, C.O. Kappe, *J. Flow Chem.* **2020**, *10*, 475-490.
25. S. Gisbertz, B. Pieber, *ChemPhotoChem*, **2020**, *4,* 456.
26. (a) H.P.L. Gemoets, Y. Su, M. Shang, V. Hessel, R. Luque, T. Noël, *Chem. Soc. Rev.* 2016, 45, 83-117. (b) C.A. Hone, D.M. Roberge, C.O. Kappe, *ChemSusChem* 2017, 10, 32-41.
27. D.A. Giannakoudakis, D. Łomot, J.C. Colmenares, *Green Chem*. **2020**, *22*, 4896-4905.
28. (a) Q. Zhang, Z. Dong, S. Zhao, Z. Liu, and G. Chen, *Chem. Eng. J.* **2021**, *405* 126720. (b) Z. Dong, C. Yao, Y. Zhang, G. Chen, J. Xu, Q. Yuan, *AIChE J*. **2016**, *62*, 1294-1307.
29. S. Higashimoto, N. Kitao, N. Yoshida, T. Sakura, M. Azuma, H. Ohue, Y. Sakata, *J. Catal.* **2009**, *266*, 279-285.
30. J. Yue, G. Chen, Q. Yuan, L. Luo, Y. Gonthier, *Chem. Eng. Sci*. **2007**, *62*, 2096-2108.
31. (a) Liedtke, A.-K.; Scheiff, F.; Bornette, F.; Philippe, R.; Agar, D. W.; de Bellefon, C. *Ind. Eng. Chem. Res.* **2015**, *54*, 4699-4708. (b) Liedtke, A.-K.; Bornette, F.; Philippe, R.; de Bellefon, C. *Chem. Eng. J.* **2016**, *287*, 92-102.